*Geophysical Journal* (1989) **96**, 51–64

# Ray tracing in azimuthally anisotropic media—I. Results for models of aligned cracks in the upper crust

P. M. Shearer* and C. H. Chapman†

*Bullard Laboratories, Department of Earth Sciences, University of Cambridge, Madingley Rise, Madingley Road, Cambridge CB3 0EZ, UK*

Accepted 1988 June 28. Received 1988 June 28; in original form 1988 March 1

**SUMMARY**

Ray tracing through gradients in anisotropic materials is complicated by singularities where the two quasi-shear wave slowness sheets cross or touch. Difficulties associated with such points can be removed by explicitly including polarization in the ray tracing equations. Slowness sheet and wavefront plots show the polarization and velocity behavior of various anisotropy models of aligned cracks in the upper crust. A simple scaling of the elastic tensor with depth can be shown to be approximately correct for models of aligned cracks within an isotropic host matrix with a linear velocity gradient. Ray tracing examples for models of aligned cracks within a strong vertical velocity gradient in the uppermost crust demonstrate various features of azimuthal anisotropy, including amplitude and polarization anomalies and shear-wave splitting. Quasi-shear wave polarizations typically twist along ray paths, with stronger twisting near the symmetry axis in hexagonally symmetric media. Strong anisotropy can cause unusual effects, such as ray paths which have three turning points in laterally homogeneous models.

**Key words:** ray tracing, azimuthal anisotropy, aligned cracks

## INTRODUCTION

Anisotropy is of increasing importance in seismic studies of earth structure at all depths. Observations of upper crustal anisotropy resulting from preferred crack orientation have been made for both the oceanic (e.g. Stephen 1981, 1985; White & Whitmarsh 1984; Shearer & Orcutt 1985, 1986) and the continental crust (e.g. Crampin *et al.* 1980; Booth *et al.* 1985; Crampin & Booth 1985; Crampin *et al.* 1986). Uppermost mantle anisotropy, first recognized from oceanic Pn arrivals (Hess 1964; Raitt *et al.* 1969), is now routinely observed in oceanic refraction experiments (e.g. Au & Clowes 1982; Shimamura 1984; Shearer & Orcutt 1985, 1986), and has also been observed in continental Pn studies (Bamford 1977). Indications that this mantle anisotropy extends to considerable depths are provided by surface waves studies (e.g. Forsyth 1975; Crampin & King 1977; Mitchell & Yu 1980; Kirkwood & Crampin 1981; Tanimoto & Anderson 1985) and observations of shear-wave splitting (Ando, Ishikawa & Yamazaki 1983; Ando 1984). Recently, anisotropy in the inner core has been proposed to explain anomalous PKIKP travel-time and normal mode data (Morelli, Dziewonski & Woodhouse 1986; Woodhouse, Giardini & Li 1986).

Most of the studies mentioned above have used comparatively simple travel-time or polarization analysis. Recent developments regarding the computation of synthetic seismograms for anisotropic media (e.g. Booth & Crampin 1983; Fryer & Frazer 1984) promise that future studies will begin to use more of the full seismic waveform. However, such calculations require large amounts of computer time (many factors greater than for isotropic media), so their use is not yet routine. For this reason, concurrent development of relatively simple ray theoretical methods of modelling anisotropy is important, both for understanding the results of the full synthetic calculations and to provide first-order models of earth structure.

Our purpose in this paper will be to show examples of ray tracing for azimuthally anisotropic media with a steep vertical velocity gradient (such as might be appropriate for models of vertical cracks in the uppermost crust), with the purpose of understanding the predicted travel-time, amplitude and polarization anomalies. A significant result of this analysis is that quasi-shear wave polarizations typically twist along ray paths, with stronger twisting near the symmetry axis of hexagonal material. This causes coupling between the quasi-shear waves, which is discussed in Chapman & Shearer (1989, henceforth referred to as Paper II).

## RAY TRACING THEORY

This section first briefly summarizes results from Červený (1972) and Červený, Molotkov and Pšenčík (1977) and then discusses the problem of tracing rays near points where the shear-wave slowness sheets come together.

* Now at: Institute of Geophysics and Planetary Physics, Scripps Institution of Oceanography, U.C. San Diego, La Jolla, CA 92093.
† Now at: Department of Physics, University of Toronto, Toronto, Ontario M5S 1A7, Canada.

The eigenvalue equation for anisotropic media may be expressed as

$$(a_{ijkl}\hat{p}_j\hat{p}_l - v^2\delta_{ik})\hat{g}_k = 0, \tag{1}$$

where $\mathbf{a}$ is the density normalized elastic tensor, $\hat{\mathbf{p}}$ is the slowness unit vector, $\hat{\mathbf{g}}$ is the polarization unit vector, and $v$ is the phase velocity. Defining the slowness vector $\mathbf{p} = \hat{\mathbf{p}}/v$, and the Christoffel matrix $\Gamma_{ik} = a_{ijkl}p_jp_l$, we can rewrite this as

$$(\Gamma_{ik} - G\delta_{ik})\hat{g}_k = 0, \tag{2}$$

where $G = 1$ represents a solution to (1). Equation (2) has a non-trivial solution only when one of the eigenvalues of the matrix $\boldsymbol{\Gamma}$ ($G_1$, $G_2$ or $G_3$) is equal to one. These three solutions correspond to a quasi-compressional wave and two quasi-shear waves. We thus have the system of non-linear partial differential equations $G_m(p_i, x_i) = 1$, which can be solved by the method of characteristics (Červený 1972) and expressed as

$$\frac{dx_i}{d\tau} = \frac{1}{2}\frac{\partial G_m}{\partial p_i}, \qquad \frac{dp_i}{d\tau} = -\frac{1}{2}\frac{\partial G_m}{\partial x_i}, \qquad i = 1, 2, 3. \tag{3}$$

This system of ordinary differential equations could be used for ray tracing. However, a more convenient form for these equations may be derived by finding expressions for the partial derivatives of the eigenvalues $G_m$. The resulting equations are (see Červený 1972 for details of the derivation and expressions for $D_{ij}$)

$$\begin{aligned} \frac{dx_i}{d\tau} &= a_{ijkl}p_lD_{jk}/D, \\ \frac{dp_i}{d\tau} &= -\frac{1}{2}\frac{\partial a_{ljks}}{\partial x_i}p_lp_sD_{jk}/D, \qquad i = 1, 2, 3. \end{aligned} \tag{4}$$

This system of equations is completely general and suitable for numerical solution (i.e. ray tracing) provided $a_{ijkl}$ and its spatial derivatives are known and finite throughout the region of interest. Initial conditions for $\mathbf{x}$ and $\mathbf{p}$ must be specified which satisfy $G_m(\mathbf{p}, \mathbf{x}) = 1$; it is these initial conditions which specify the ray type (i.e. quasi-compressional or one of the two quasi-shear waves). A second-order Runge–Kutta method was used for the ray tracing examples in this paper.

No problems will occur when these equations are used for quasi-compressional ($qP$) waves. However, difficulties arise for quasi-shear ($qS$) waves when the two shear-wave slownesses coincide. In this case, the eigenvalues are degenerate, the denominator term $D = 0$, and the equations (4) cannot be used. This situation occurs when the two shear-wave slowness sheets cross or touch each other (see Crampin & Yedlin 1981 for a discussion regarding the nature and geometry of these slowness sheets). Although such points may be rare in the sense that they represent an infinitely small proportion of the area of the slowness sheets, they often cause trouble in ray tracing problems. In practice, numerical stability problems arise whenever the shear-wave slowness sheets come close to each other, regardless of whether they actually touch or not.

The reason that equations (4) cannot be used for the case of degenerate eigenvalues is that the expressions depend upon the polarization, which is undetermined at these points. The matrix $D_{jk}/D$ can also be expressed as the product of unit polarization vectors (i.e. Červený & Firbas 1984; Gajewski & Pšenčík 1987):

$$D_{jk}/D = \hat{g}_j\hat{g}_k \tag{5}$$

and equations (4) rewritten as

$$\begin{aligned} \frac{dx_i}{d\tau} &= a_{ijkl}p_l\hat{g}_j\hat{g}_k, \\ \frac{dp_i}{d\tau} &= -\frac{1}{2}\frac{\partial a_{ljks}}{\partial x_i}p_lp_s\hat{g}_j\hat{g}_k, \qquad i = 1, 2, 3. \end{aligned} \tag{6}$$

These equations can be used even at points where the slowness sheets cross, provided the polarization is known. All the ray tracing examples in this paper involve hexagonally symmetric anisotropy, for which there are relatively simple expressions for the wave polarization (see Appendix), which can be used directly in (6). Generally little difficulty is caused by situations in which the slowness sheets cross, provided that the polarizations on the sheets are not changing rapidly with respect to position (such as at intersection singularities in hexagonally symmetric materials). However, strange results can occur at or near singularities in the polarization (such as occur for $qS$-waves on the symmetry axis of a hexagonally symmetric material). In these regions the polarizations can change very rapidly along the ray paths, and the results predicted by ray tracing will generally be incorrect because of the coupling which occurs between the quasi-shear waves (see Paper II).

## ANISOTROPY MODELS

The ray tracing equations discussed in the previous section are very general and can be used for any desired three-dimensional continuous distribution of the 21 independent components of the elastic tensor, which clearly allows for extremely complicated models. However, we will consider only simple models of hexagonally symmetric media with properties which vary only with depth. More complex anisotropy models are certainly possible, but hexagonal symmetry is suitable for studying most forms of anisotropy which have actually been observed in the earth (i.e. aligned cracks, periodic thin layering, preferred orientation of a single crystal axis). Despite their relative simplicity, these models are sufficient to demonstrate many of the unusual features of anisotropic wave propagation. The restriction to hexagonally symmetric material still allows for seven independent anisotropic parameters (five plus the symmetry axis direction), a substantial increase from the two parameters of isotropic material.

The anisotropy models are derived from theoretical expressions for the elastic response of a material containing cracks (Hudson 1980, 1981), and demonstrate the effect on seismic velocities of aligned ellipsoidal cracks within a host rock (see Crampin 1984 for other examples of aligned crack models). These models are characterized by the elastic properties of the host matrix and the material in the cracks, and two additional parameters, the crack aspect ratio and crack density. The crack aspect ratio $d$ is the ratio of crack thickness to crack diameter. The crack density $\epsilon$ is the number of cracks per unit volume and is defined as $\epsilon = Na^3/V$, where $N$ is the number of cracks per volume $V$, and $a$ is the crack radius. The Hudson (1980) theory is valid at small values of crack aspect ratio and density ($d$, $\epsilon \ll 1$).

These aligned crack models may be appropriate for modelling observations of crack-induced upper crustal anisotropy (e.g. Stephen, 1981, 1985; Booth *et al.* 1985; Crampin & Booth 1985; Crampin *et al.* 1986; Shearer & Orcutt 1985, 1986). Leary, Li & Aki (1987) and Li, Leary & Aki (1987) recently used the Hudson theory and anisotropic ray tracing to model vertical seismic profile data showing fault zone anisotropy. We consider four examples which illustrate the different kinds of anisotropy produced by aligned cracks. In all cases, the isotropic host rock was assumed to have properties ($\alpha = 4.5\,\mathrm{km\,s^{-1}}$, $\beta = 2.53\,\mathrm{km\,s^{-1}}$, $\sigma = 0.27$, $\rho = 2.8\,\mathrm{Mg\,m^{-3}}$) typical of the uppermost crust. Figs 1–4 show slowness sheets and wavefronts (i.e. group velocity) for each model.

Wave polarization vectors are indicated by the arrows on the slowness sheet figures in order to illustrate the behaviour of the quasi-shear waves. Following Backus (1970), the arrows are drawn with conical tips in order to show all three

Model 1: Thin wet cracks

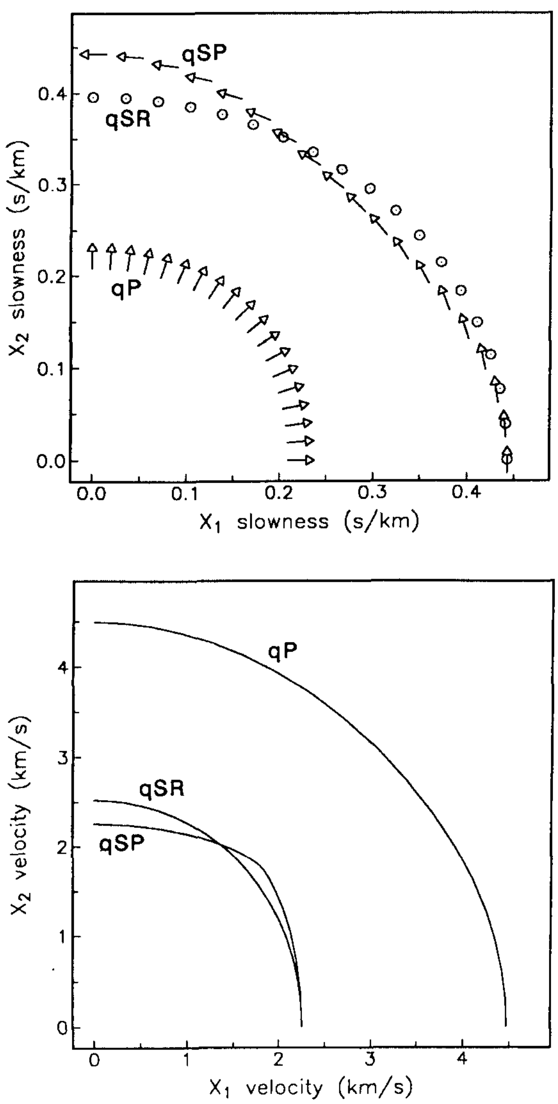


**Figure 1.** Slowness sheets, polarizations, and wavefronts for Model 1 (thin water-filled cracks, $d = 0.001$, $\epsilon = 0.1$). Polarizations are indicated by arrows with conical tips; the q*SR*-wave polarizations are perpendicular to the plane of the paper.

Model 2: Thick wet cracks

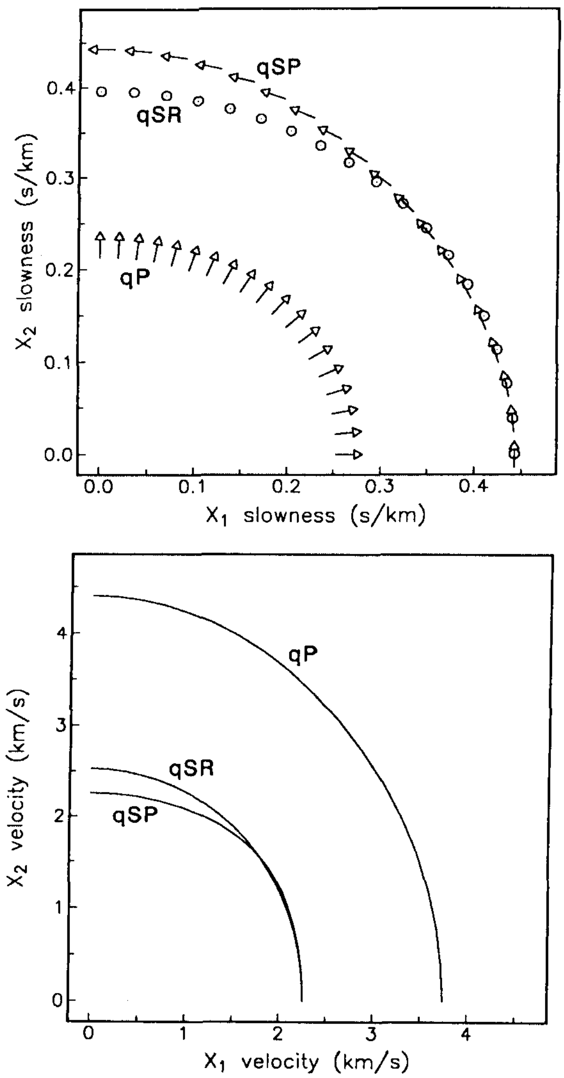


**Figure 2.** Slowness sheets, polarizations, and wavefronts for Model 2 (thick water-filled cracks, $d = 0.1$, $\epsilon = 0.1$).

components of the polarization vector; thus polarizations which are perpendicular to the plane of the drawing appear as circles with central dots. Following the notation of Crampin (1981), the wave types are labelled as q*P* for quasi-*P*, q*SP* for quasi-*S* with polarization within a symmetry plane, and q*SR* for quasi-*S* with polarization orthogonal to the symmetry plane. This notation is unambiguous for hexagonally symmetric media, for which a symmetry plane can be found for every point on the slowness surfaces. For such hexagonally symmetric media, q*P*-wave velocities vary approximately as a $2\theta$ and $4\theta$ function of angle from the symmetry axis, q*SP*-waves vary as a $4\theta$ function, and q*SR*-waves vary as a $2\theta$ function (Crampin 1981). For transversely isotropic media (i.e. hexagonally symmetric with a vertical symmetry axis), q*SP* corresponds to q*SV*, while q*SR* corresponds to q*SH*. The full three-dimensional nature of the slowness sheets and wavefront surfaces may be visualized by imagining the surfaces rotated about the $x_1$-axis, the symmetry axis in these plots (i.e. the cracks are parallel to the $x_2 - x_3$ plane).

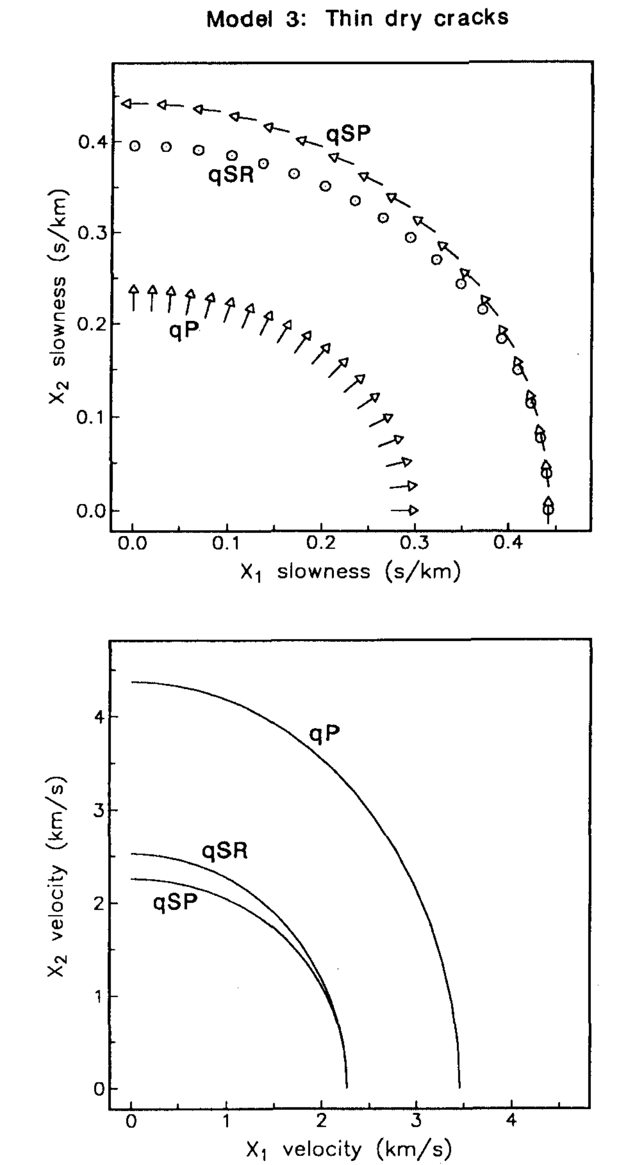


**Figure 3.** Slowness sheets, polarizations, and wavefronts for Model 3 (thin dry cracks, $d = 0.001$, $\epsilon = 0.1$).

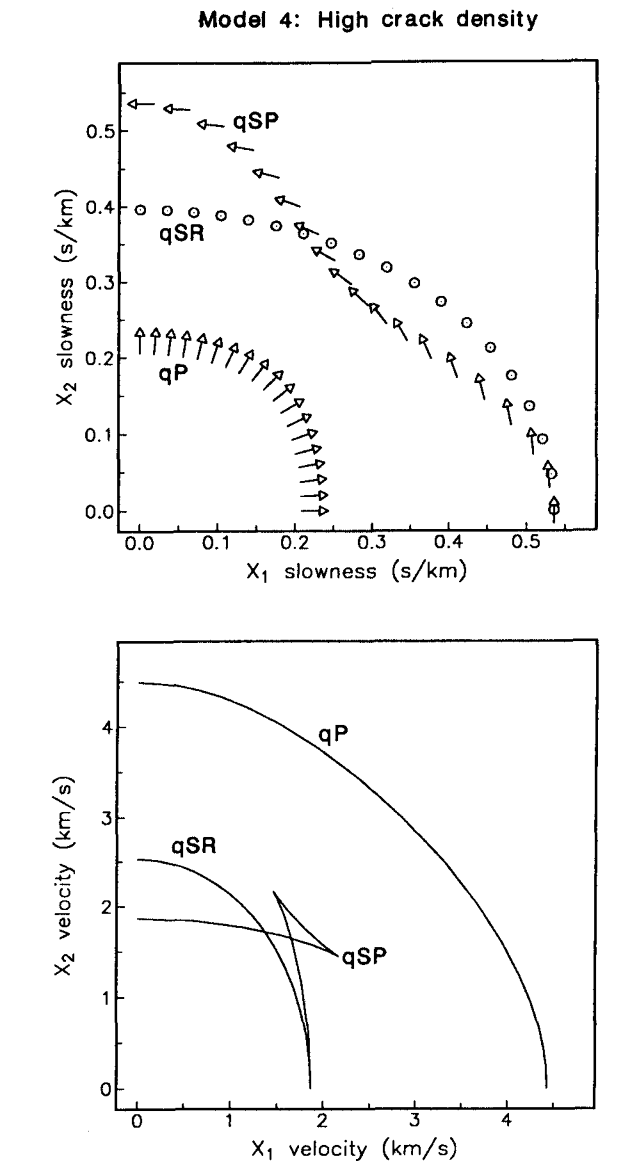


**Figure 4.** Slowness sheets, polarizations, and wavefronts for Model 4 (thin water-filled cracks, extremely anisotropic, $d = 0.001$, $\epsilon = 0.3$). Notice the concave outward part of the q*SP*-wave slowness sheet which causes the cusps in the q*SP* wavefront.

### 1. Thin water-filled cracks

The model material contains aligned, vertical, water-filled cracks with crack aspect ratio $d = 0.001$ and crack density $\epsilon = 0.1$. Density normalized elastic constants of the model are: $a_{1111} = 20.04$, $a_{2222} = 20.22$, $a_{1212} = 5.10$, $a_{2323} = 6.38$, $a_{1122} = 7.41\ \mathrm{km^2\,s^{-2}}$. This is similar to model HCS1 of Crampin (1984), except slower velocities are assumed for the host rock. Slowness sheets and wave fronts are shown in Fig. 1. q*P*-wave anisotropy [defined as $(V_{\max} - V_{\min})/V_{\mathrm{avg}}$] is 3.5 per cent; q*SP*- and q*SR*-wave anisotropy is 11.2 per cent. q*P*- and q*SP*-wave velocities vary as a $4\theta$ function of azimuth; q*SR*-wave velocities vary as a $2\theta$ function of azimuth. Notice that the q*S*-wave slowness sheets touch along the symmetry axis and cross at an angle of about 60° from the symmetry axis. The q*SP*-wave slowness sheet is flattened (but never concave outward) near 45°, causing a sharp angle in the q*SP* wavefront.

### 2. Thick water-filled cracks

This model is identical to Model 1, except that the crack aspect ratio is assumed to be 0.1 rather than 0.001. This change from thin to thick cracks has a significant effect on the elastic properties of the material, as noted by Anderson, Minster & Cole (1974), Shearer & Orcutt (1986) and Crampin, McGonigle & Ando (1986). Elastic constants of the model are: $a_{1111} = 14.02$, $a_{2222} = 19.40$, $a_{1212} = 5.10$, $a_{2323} = 6.38$, $a_{1122} = 5.18\ \mathrm{km^2\,s^2}$. Relative to Model 1, q*SR*-wave anisotropy is unaffected, but q*P*-wave anisotropy increases to 16.2 per cent with a mainly $2\theta$ azimuthal dependence, and q*SP*-wave anisotropy decreases to 6.1 per cent. Quasi-shear wave phase and group velocities are nearly identical at angles up to 45° from the symmetry axis. Ray tracing using equation (4) proved to be numerically unstable throughout this region, while equations (6) gave accurate results.

**3. Thin dry cracks**

This model is identical to Model 1, except that the cracks are now assumed to be dry, rather than water-filled. Dry crack models differ significantly from wet crack models, as discussed by Crampin (1984). Elastic constants of the model are: $a_{1111} = 11.91$, $a_{2222} = 19.11$, $a_{1212} = 5.10$, $a_{2323} = 6.38$, $a_{1122} = 4.40\,\mathrm{km}^2\,\mathrm{s}^{-2}$. Relative to Model 1, q*P*-wave anisotropy increases to 24 per cent with a mainly $2\theta$ azimuthal dependence, q*SP*-wave anisotropy decreases to 4.3 per cent, and q*SR*-wave anisotropy is unaffected. q*SR*-waves are faster than q*SP*-waves at all angles except where the slowness sheets touch along the symmetry axis. Generally, however, the q*S*-waves in this model are similar to those in Model 2, the main differences being in the q*P*-waves. The obvious fourth combination, thick dry cracks, does not differ significantly from the thin dry crack model.

**4. Thin water-filled cracks (extremely anisotropic)**

This model is identical to Model 1, except that the crack density is assumed to be 0.3 rather than 0.1. Although such a large crack density may exceed the valid range of the Hudson (1980) theory, this model is included to illustrate some of the unusual properties of extremely anisotropic models. Elastic constants of the model are: $a_{1111} = 19.63$, $a_{2222} = 20.16$, $a_{1212} = 3.48$, $a_{2323} = 6.38$, $a_{1122} = 7.26\,\mathrm{km}^2\,\mathrm{s}^{-2}$. q*P*-wave anisotropy is 15 per cent with a $4\theta$ azimuthal dependence, q*SP*-wave anisotropy is 30 per cent with a $4\theta$ dependence, and q*SR*-wave anisotropy is 29 per cent with a $2\theta$ dependence. The q*SP*-wave slowness sheet is concave outward at angles between about 30° and 60° from the symmetry axis, causing cusps in the wave front, and a multi-valued group velocity function. These cusps are associated with many unusual wave propagation features (see, for example, Crampin 1981). They begin to occur for the Hudson (1980) model of aligned cracks at crack densities of about 0.13. For hexagonally symmetric models, they can only occur for q*SP*-waves and never for q*SR*-waves, since it is the $4\theta$ angle dependence which causes them. The q*P*-wave slowness sheet is never concave outward (for a simple proof, see Payton 1983).

## ANISOTROPY DEPTH SCALING

For simplicity, we assume that the above models represent elastic properties at the surface of the crust, and that these properties change only with depth. Further, we assume that the elastic properties vary only by a simple scalar factor, so that the elements of the elastic tensor are always in the same proportion to each other. This has great advantages in understanding the results of the ray tracing, since the figures describing the models (1–4) are applicable at any depth, if the appropriate scaling factor is applied. Finally, we assume that the elastic tensor varies quadratically with depth, so that the corresponding velocity gradient is linear (Shearer & Chapman 1988). In this case, we can obtain the elastic tensor, $a_{ijkl}$, at a particular depth from

$$a_{ijkl}(z) = a_{ijkl}(z_0)[1 + \alpha'(z - z_0)/\alpha_0]^2, \tag{7}$$

where $\alpha_0$ is the *P*-wave velocity at depth $z_0$, and $\alpha'$ is the effective *P*-wave velocity gradient. For all examples in this paper we assume $\alpha' = 1\,\mathrm{s}^{-1}$, a relatively steep velocity gradient which may be appropriate for the uppermost crust. We define $\alpha_0$ as the *P*-wave velocity from the isotropic part of the elastic tensor (see Backus 1982), but the simpler method of averaging the minimum and maximum velocities would give very similar results.

Although this form of the model depth dependence was largely chosen for convenience, it may also be a reasonable approximation to upper crustal anisotropy in the earth. Fig. 5 compares Model 2 q*P*- and q*S*-wave velocities vs. depth obtained from equation (7) with those calculated for the Hudson (1980) aligned crack model, assuming a linear velocity gradient in the host matrix. Both models predict an increase in anisotropy with depth, although the equation (7) model predicts slightly less q*P*-wave anisotropy and slightly lower q*S*-wave velocities. It is doubtful whether these differences could be distinguished with real data considering the often noisy nature of upper crustal seismic observations.

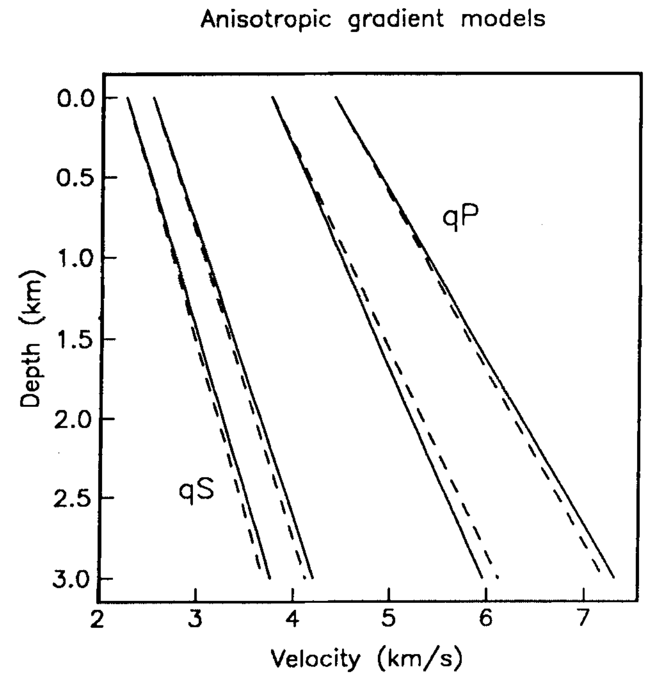


**Figure 5.** Maximum and minimum q*P*- and q*S*-wave velocities as a function of depth for the Hudson (1980) crack theory (solid lines) and a simple scaling of the elastic tensor (dashed lines). A linear velocity gradient in the host matrix is assumed for the crack model.

## RAY TRACING RESULTS

The depth scaling of the anisotropy in these examples makes it easy to correlate the ray tracing results with properties of the model slowness sheets shown in Figs 1–4. This is illustrated in Fig. 6 which compares an individual q*SR*-wave ray path with a vertical cross-section of the appropriate slowness sheet from Model 1. The ray is initially defined with a slowness vector azimuth of 45° from the symmetry axis at an angle of 45° from vertical. A cross-section of the

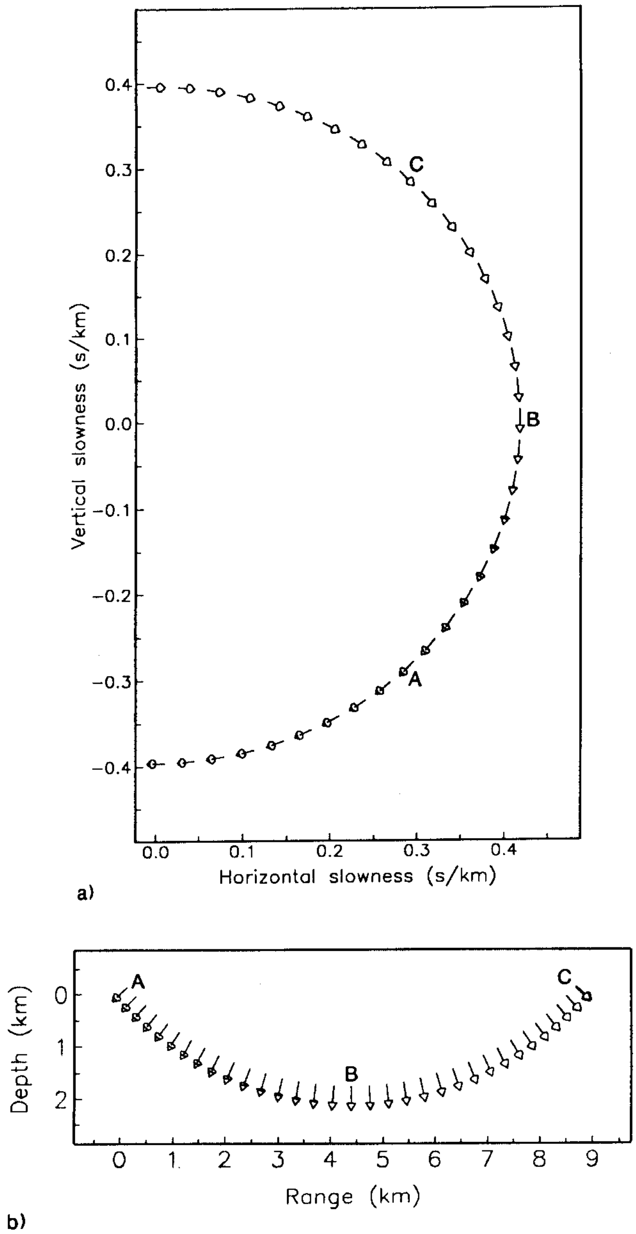


**Figure 6.** A cross-section of a q$SR$-wave ray path (b) compared with the corresponding vertical cross-section of the q$SR$-wave slowness sheet (a). Points A, B and C along the ray path are associated with corresponding points on the slowness sheet. Arrows are shown at 0.1 s intervals along the ray path, except for the final point at the surface.

resulting ray path is shown in Fig. 6b. Arrows indicate the wave polarization and are spaced at 0.1 s intervals. The ray turns at a depth of about 2 km and arrives at the surface at a range of about 9 km. Fig. 6a shows a vertical cross-section (45° from the symmetry axis) of the q$SR$-wave slowness surface for Model 1 at the surface.

Points along the ray path may be correlated with the slowness sheet as follows: the point labelled A shows the position of the source. The slowness vector points down at an angle of 45°. The group velocity (ray direction) at this point is indicated by the normal to the slowness surface (remember that the arrows in Fig. 6 indicate wave polarizations, not group velocity vectors). Notice that this is generally different from the slowness vector direction. As the ray moves downward, the model velocities increase, causing the slowness surface shown in Fig. 6a to shrink. Because horizontal slowness must be conserved, this will cause the ray path to move up along the slowness surface from point A. For the examples in the paper, the elastic constants vary with depth by a scalar factor, so the shape of the slowness curve remains the same. Thus, a convenient way of visualizing the ray path along the slowness sheet is to imagine that the slowness sheet is fixed in size and shape, but that the horizontal slowness of the ray increases with depth. For the particular depth scaling of the elastic tensor described by equation (7), the ray path is *exactly* the same shape as the corresponding slowness sheet rotated by 90° (Shearer & Chapman 1988).

As we move up along the slowness sheet from point A, the ray direction becomes more shallow, until at point B, the turning point, the ray is travelling horizontally. For this example, the vertical slowness is zero at this point, but this will not generally be true for other models (with non-horizontal symmetry axes). Using similar arguments, we can trace the ray along the slowness sheet back up to the surface at point C. The ray is vertically polarized at the turning point, but twists out of the plane of the cross-section at other points along the ray path.

Figure 7 compares this q$SR$ ray path with q$P$ and q$SP$ ray paths for the same model and slowness direction. The faster q$P$ velocities can be seen in the greater spacing of points along its ray path. q$P$ polarizations deviate slightly from the ray direction, but not enough to be visible in Fig. 7. q$SP$ and q$SR$ polarizations both twist in a counter-clockwise direction continuously along the ray path, remaining orthogonal to

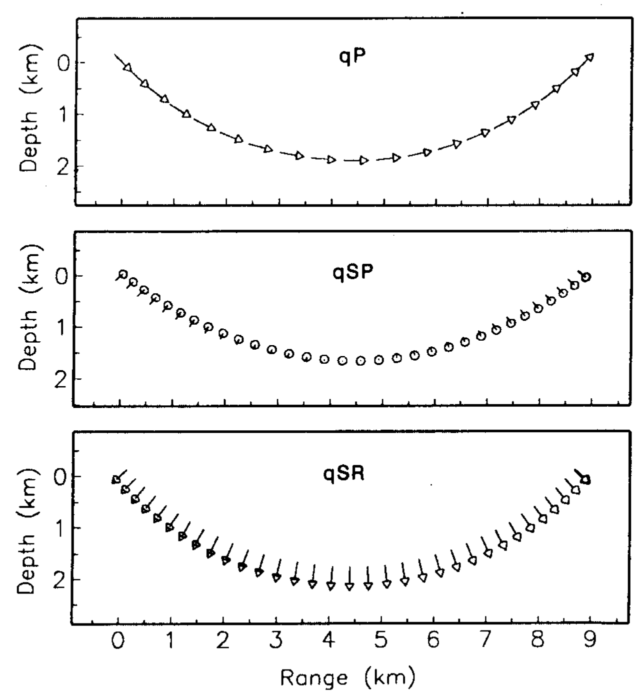


**Figure 7.** A comparison of q$P$-, q$SP$- and q$SR$-wave ray paths and polarizations. Arrows are shown at 0.1 s intervals along the ray path, except for the final surface points. q$SP$- and q$SR$-wave polarizations twist significantly along the ray path.

each other. This twisting of the q*S*-wave polarizations indicates that there will be coupling between the shear waves (see Paper II): for these examples it is assumed that the frequencies are sufficiently high that coupling is not important.

Figure 8 shows a plan view of q*P*, q*SP*, and q*SR* ray paths for Model 1 at azimuths of 0° to 90° (5° spacing) from the $x_1$ symmetry axis. Points are shown every 0.1 s along the ray paths. q*SP* rays are concentrated near an azimuth of 45°, reflecting the flattening of the q*SP* slowness surface (see Fig. 1). Close examination of the ray paths reveals that they are slightly curved, and not generally confined to a vertical source–receiver plane, despite the fact that the model parameters vary only with depth. This deviation of the ray path from the source-receiver plane was discussed by Shearer & Orcutt (1985). q*SP* and q*SR* polarizations change very rapidly near the turning point for rays close to the $x_1$ symmetry axis. Notice that the q*S*-wave polarizations change abruptly by 180° at the turning point for the rays which turn along the symmetry axis. This results from the singularity in the polarizations at the symmetry axis, the implications of which are discussed in Paper II.

In order to predict the polarization and travel-time anomalies which might be observed at the surface, we calculated ray paths at increments between 0° to 90° in azimuth and 45° to 80° in incidence angle for each model. The results are shown for each of the four models in Figs 9–12. Because of the symmetry of the models, the results at other azimuths (i.e. 90° to 360°) are mirror images of these plots. The polarization of each upcoming ray at the receiver is indicated by the arrows, with each arrow representing an entire ray path. This polarization does not necessarily

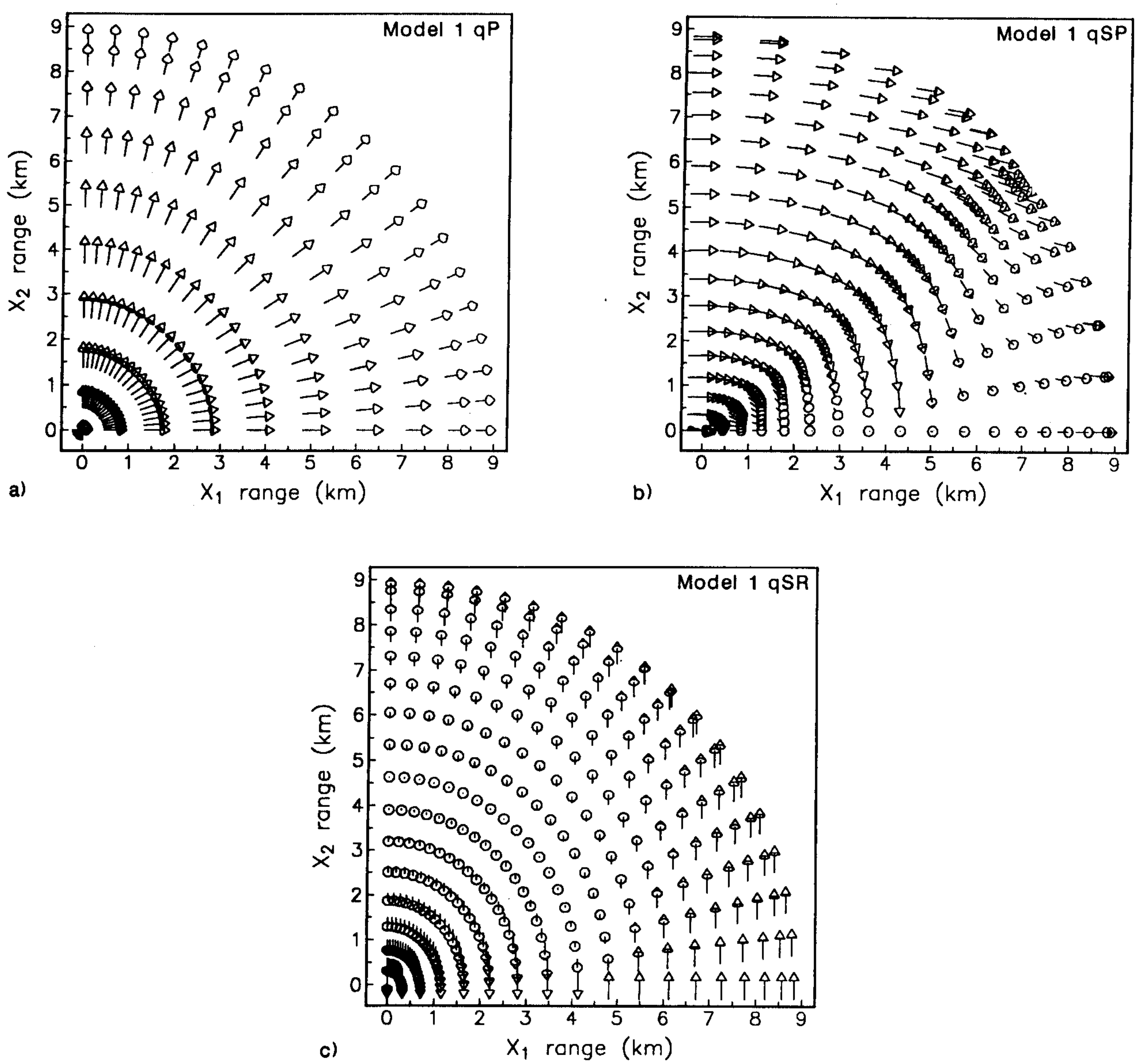


**Figure 8.** Ray paths for Model 1 at azimuths between 0° and 90° from the symmetry axis ($x_1$). Each ray leaves the source at a phase angle of 45° from vertical. Arrows are shown at 0.1 s intervals along the ray path, except for the final points at the surface. Notice the bunching of the q*SP*-wave rays near an azimuth of 40° from the symmetry axis; this results from the flattened part of the Model 1 q*SP* slowness surface (see Fig. 1). Also notice the singularity in the q*SP*- and q*SR*-wave polarizations at 4.5 km range along the $x_1$ symmetry axis.

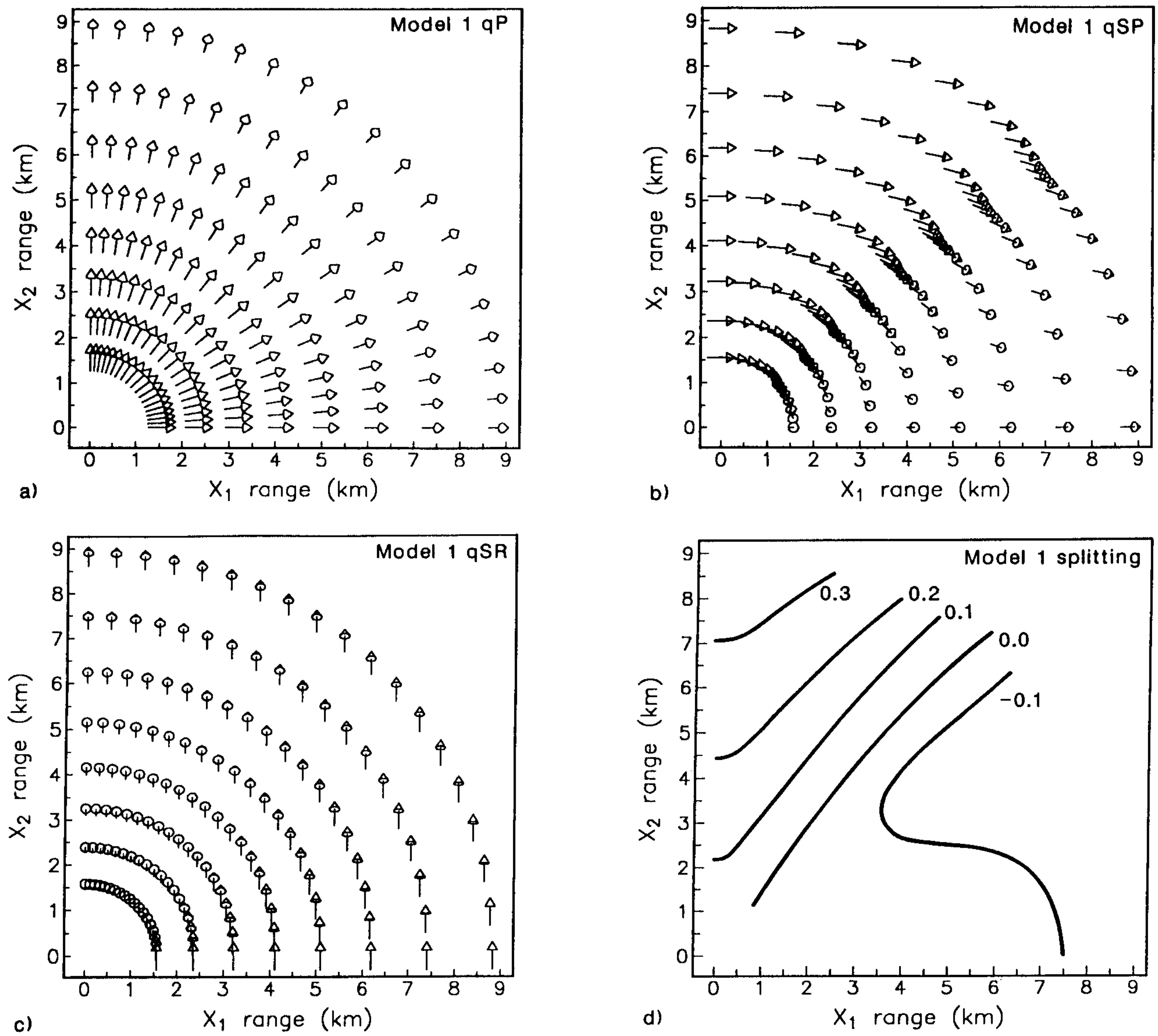


**Figure 9.** Surface polarizations for Model 1 (thin, water-filled cracks). Each arrow represents the end point of an entire ray path. Rays are evenly spaced between 0° and 90° in phase azimuth and 45° and 80° in phase angle from vertical. (d) contours the time delay between the q*SP*- and q*SR*-wave arrivals (i.e. the shear-wave splitting). Positive times correspond to points at which q*SR* arrives first, negative times to points at which q*SP* arrives first.

represent the actual particle motion at the surface, because of the complication of surface-reflected phases (as discussed in Booth & Crampin 1985). For each model, q*P*-, q*SP*-, and q*SR*-waves are shown by Figs a, b, and c, respectively. Fig. d shows the travel-time difference between the quasi-shear wave arrivals (the shear-wave splitting) in 0.1 s contours.

For each of the models shown, q*P*-wave polarization anomalies are small (as discussed by Crampin, Stephen & McGonigle 1982). q*SP* and q*SR* polarizations vary with ray azimuth and incidence angle. Near the $x_1$ symmetry axis, q*SR* polarizations correspond to *SH* and q*SP* polarizations correspond to *SV*, but this relationship is reversed at azimuths near 90° away from the symmetry axis. At intermediate azimuths, the quasi-shear wave polarizations are skewed relative to the ray path and correspond to neither *SH*- or *SV*-waves.

Figure 9 shows ray tracing results for Model 1 (thin wet cracks). The arrivals are generally evenly spaced except for the concentration of q*SP*-wave arrivals at azimuths near 45°. As previously discussed, this is a result of the flattening of the q*SP* slowness sheet at these angles, which causes nearly identical group velocity (ray) directions for a range of slowness directions. Thus, higher q*SP* amplitudes should be expected at this azimuth, although of course these amplitudes also depend upon the radiation pattern of the source. If the source were in an overlying isotropic layer and the energy equally distributed in angle, the focusing shown in Fig. 9b is directly applicable. Shear-wave splitting of up to 0.37 s is shown in Fig. 9d. q*SR*-waves arrive first at azimuths between about 50° and 90° from the symmetry axis, with q*SP*-waves arriving first at smaller azimuths. The time separation is generally greater when the q*SR*-waves arrive

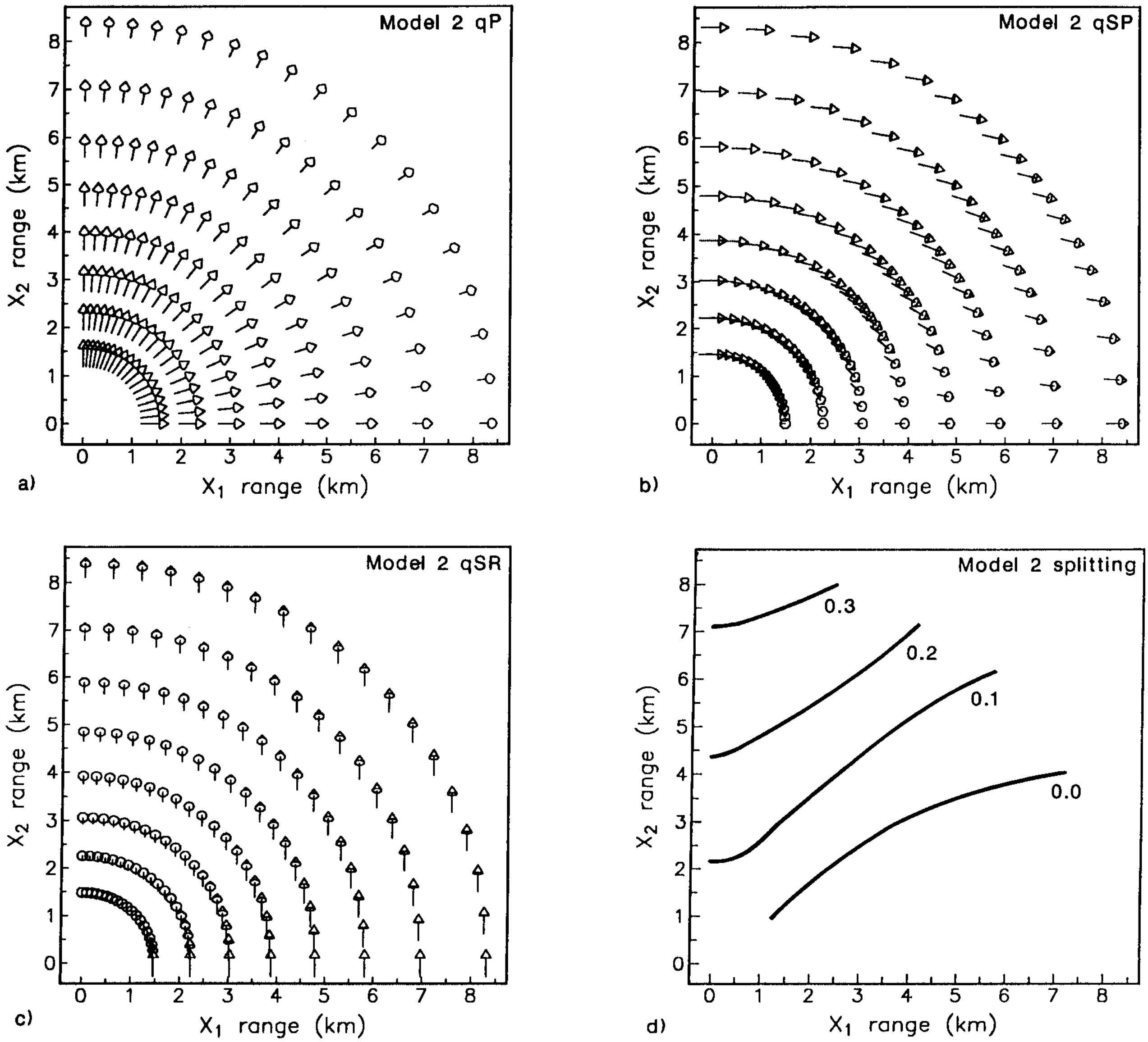


**Figure 10.** Surface polarizations for Model 2 (thick, water-filled cracks). See Fig. 9 for plot description.

first with the maximum splitting occurring at 90° from the symmetry axis. A smaller maxima occurs at an azimuth of about 35°, for which the q*SP*-wave arrives first.

Figure 10 shows the predicted polarization and shear-wave splitting pattern for Model 2 (thick wet cracks). Relative to Fig. 9, the main differences are that the focusing of the q*SP*-waves is reduced, and the quasi-shear waves arrive at nearly the same time at azimuths between 0° and about 30° to 40° (note the range dependence). If the time separation between the q*S*-waves is less than the dominant period of the data, the particle motion would be elliptical at these azimuths, with distinct shear-wave arrivals apparent only at greater azimuths. The predicted polarizations and shear-wave splitting for Model 3 (thin dry cracks), shown in Fig. 11, are very similar to the Model 2 results, the main difference being in the q*P*-wave travel times.

Figure 12 shows a more interesting example from Model 4, the extremely anisotropic model. In this case, rays are shown at increments of 2.5° in azimuth and 7° in incidence angle in order to properly illustrate the loops in the q*SP*-wave arrivals. These loops result from the concave outward part of the q*SP*-wave slowness sheet for this model, and are associated with the cusps in the wavefront (see Fig. 4). At azimuths between about 30° and 50°, there is a triplication in the q*SP*-wave arrivals, in which three different branches can be seen. Amplitudes throughout this region should be enhanced, with amplitude peaks associated with the caustics at azimuths of about 30° and 50°. Arrivals on the retrograde branch between these caustics will be Hilbert transformed relative to the forward branch arrivals (Duff 1960; Singh & Chapman 1986). The polarizations differ somewhat between the branches, so the observed particle motions in this region will be very complicated. For this reason, a shear-wave splitting plot is not shown for this model.

These plots are examples of the kinds of polarization

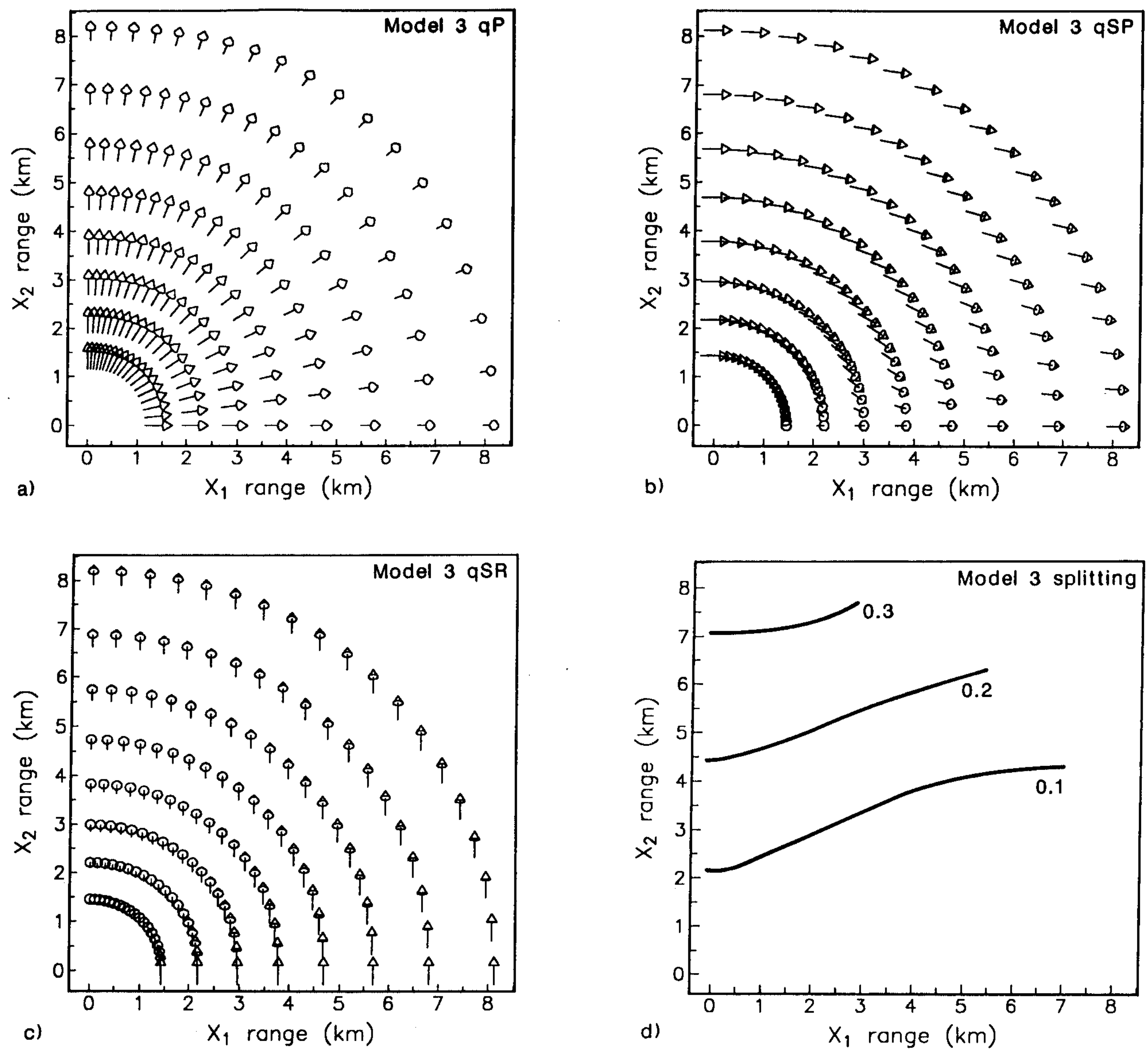


**Figure 11.** Surface polarizations for Model 3 (thin, dry cracks). See Fig. 9 for plot description.

anomalies which might be expected for a source and receiver above an anisotropic layer in which velocities increase sharply with depth. Such models may be appropriate for crack-induced anisotropy in the uppermost crust, and are more realistic than simple calculations for a homogeneous anisotropic layer [used by Crampin & Booth, (1985) and Stephen (1985) to model *S*-wave splitting observations]. This ray tracing technique (i.e. equations 6) could easily be generalized to include buried sources or receivers, and overlying or underlying isotropic layers. In the case of models with discontinuities, reflection and transmission coefficients could be calculated in order to make first-order estimates of ray amplitudes (as suggested by Stephen 1985) and properly account for any free surface effects (as discussed by Booth & Crampin 1985). However, because of coupling between the quasi-shear waves, the shear-wave polarizations which we have shown here will only be accurate at relatively high frequency (see Paper II).

## TRIPLE TURNING POINT EXAMPLE

Ray paths in anisotropic material can sometimes appear strange, if one is used to seeing ray paths in isotropic material. As an example, Fig. 13b shows a ray path for Model 4, with the model rotated 48° about the $x_2$ axis. This would correspond to an aligned crack model in which the cracks dip at 42°. Properties of the model vary only with depth. The q*SP*-wave ray path shown is for a source slowness vector at an incidence angle of 20° and at the same azimuth as the symmetry axis. For comparison, a cross-section of the q*SP*-wave slowness surface is shown in Fig. 13a. Notice that the slowness sheet is concave outward along both the horizontal and vertical axes. Because we assumed that the anisotropic velocity gradient can be described by equation (7), the slowness sheet is exactly the same shape as the ray path rotated by 90° (Shearer & Chapman 1988).

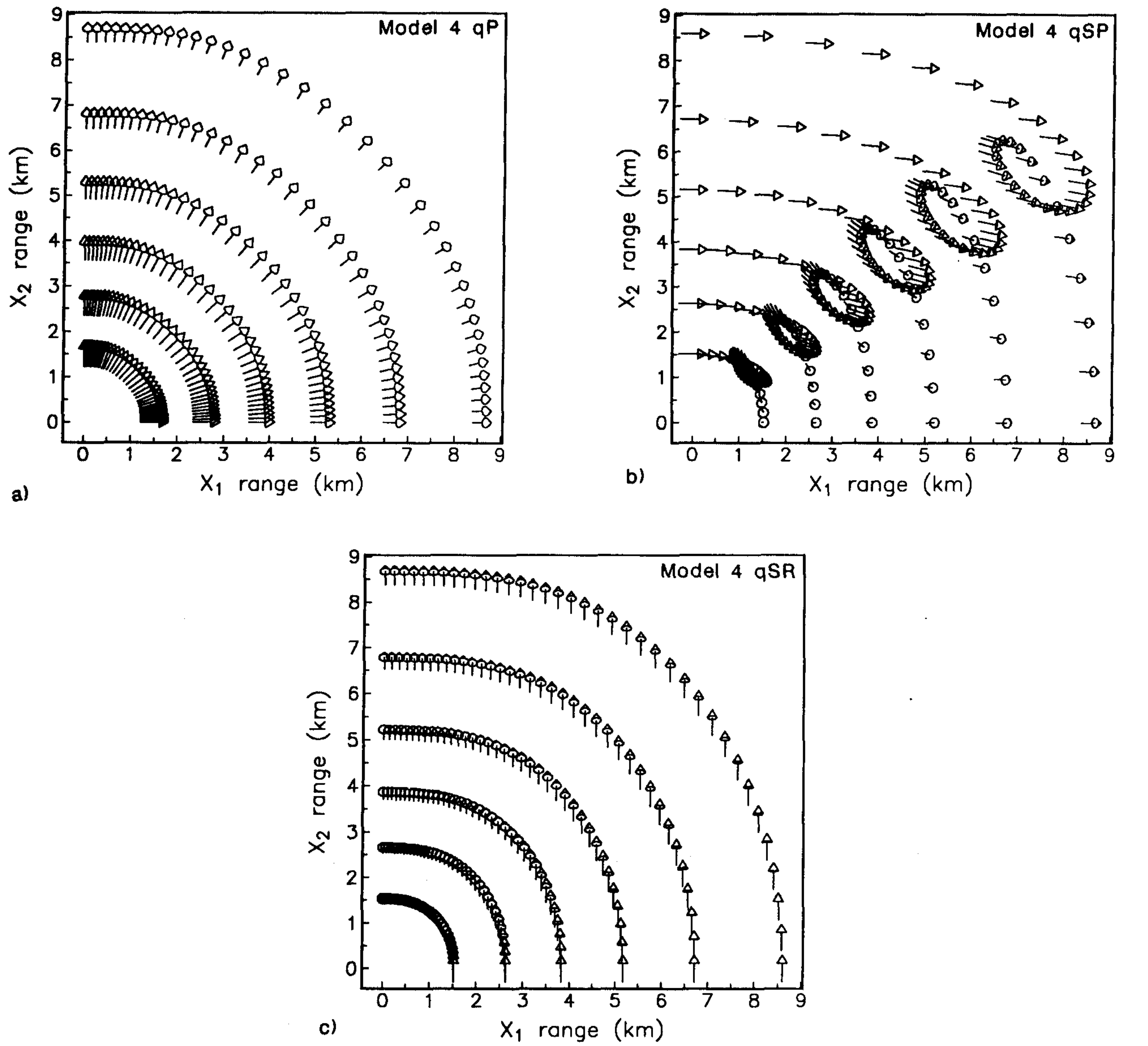


**Figure 12.** Surface polarizations for Model 4 (extremely anisotropic model of thin, water-filled cracks). See Fig. 9 for plot description. Because of the multiple q*SP*-wave arrivals, no shear-wave splitting plot is shown.

Point A corresponds to the source position on the ray path. Although the horizontal slowness is positive at this point, the group velocity vector points slightly backwards. Thus, the initial part of the ray path points away from the receiver! At point B, the ray is pointing straight down. At point C, the ray slowness vector moves through the direction of the symmetry axis of anisotropy and the ray polarization changes by 180° (this phase shift is predicted by ray theory at infinitely high frequency but will not occur at finite frequencies, see Paper II). At point D, the group velocity direction is horizontal, even though the vertical slowness is still negative. The ray turns at this point and begins going up. However, at point E, the ray turns again and begins going down. At point F, the ray turns a third time and goes up. The slowness corresponding to point G is not on the symmetry axis, so the polarization does not change at this point. At point H, the ray is going straight up. Finally, at point I, the ray arrives at the surface, with the final part of the ray path pointing slightly back toward the source. Each of the three turning points (D, E, and F) represents a different phase velocity direction and polarization, but none of the three points corresponds to zero vertical slowness. Garmany (1988a, b) has investigated the wave solution at such turning points in anisotropic media.

In an isotropic medium, such complicated ray paths could result from lateral heterogeneity. In this case, however, the material is laterally homogeneous and the complications arise purely from the anisotropy. Multiple turning point phenomena such as this occur when a concave outward part of the slowness surface intersects the horizontal plane. Concave outward slowness surfaces can only occur for quasi-shear waves, and only for very anisotropic materials.

Another interesting aspect of this example is illustrated in

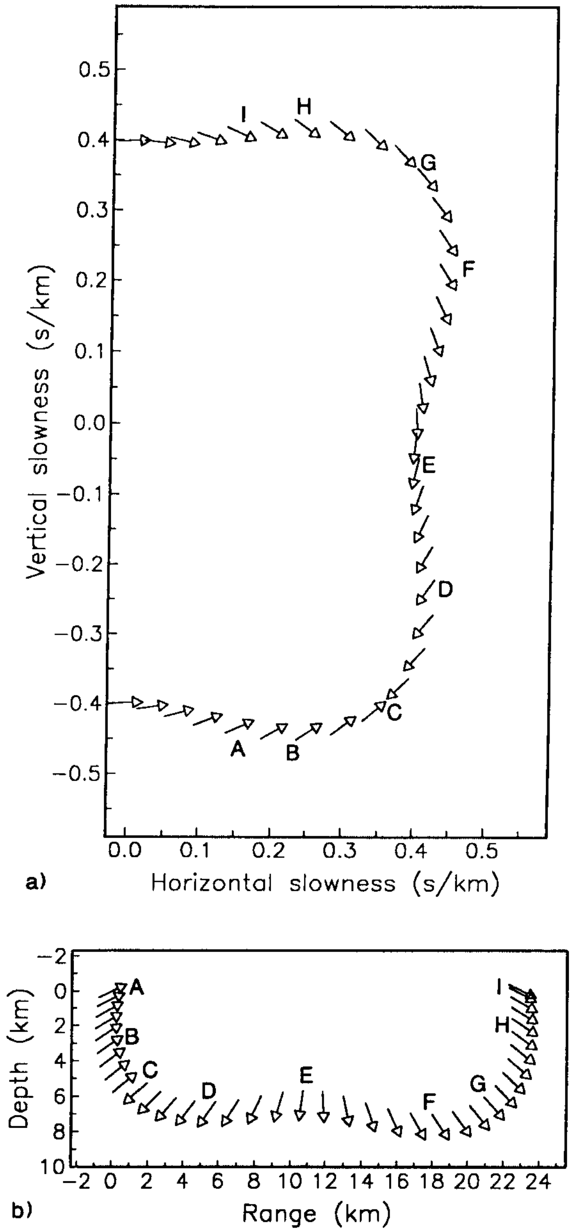


**Figure 13.** An example of a ray with three turning points. The ray path and polarizations are shown in (b), while the corresponding cross-section of the slowness sheet is shown in (a). Arrows are at 0.2 s intervals along the ray path. Points A to I along the ray path correspond with the points indicated on the slowness surface.

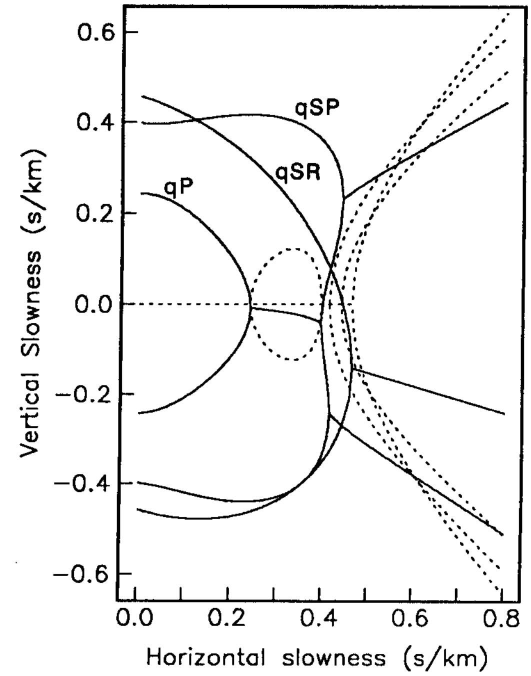


**Figure 14.** A cross-section of the q$P$, q$SP$ and q$SR$ slowness sheets for the triple turning point example shown in Fig. 13, plotting vertical slowness as a function of horizontal slowness. Real parts are shown as solid lines, imaginary parts as dashed lines. At small values of horizontal slowness, there are six purely real solutions and the slowness surfaces shown are solutions to equation (2). These represent upgoing and downgoing travelling waves with oscillatory behaviour. At large values of horizontal slowness, the waves become evanescent and the solutions occur in complex conjugate pairs. These are waves below their turning points which are decaying exponentially with depth.

Fig. 14, which plots the q$P$, q$SP$ and q$SR$ slowness sheets along the same cross-section as Fig. 13a. The plot shows the real and imaginary parts of the six eigenvalues (the vertical slownesses) for the system as a function of horizontal slowness. As noted by Keith & Crampin (1977) and Garmany (1983), these eigenvalues are either purely real or in complex conjugate pairs. At small values of horizontal slowness ($p < 0.24\,\mathrm{s\,km^{-1}}$), the six solutions are all real and correspond to upgoing and downgoing q$P$-, q$SP$- and q$SR$-waves. At larger values of $p$, the waves become evanescent and the eigenvalues are complex with increasing imaginary parts. This corresponds to the region below the ray turning point, in which amplitudes decay exponentially with depth. The intriguing aspect of this example is that there is an evanescent region *above* the middle q$SP$-wave turning point, which is linked to the evanescent region *below* the q$P$-wave turning point. At $p \simeq 0.41\,\mathrm{s\,km^{-1}}$, well past the q$P$-wave turning point, the evanescent q$P$-wave solution has disappeared and there are six real solutions, corresponding to four q$SP$-waves and two q$SR$-waves. This diagram indicates that energy may 'tunnel' through this evanescent region and cause coupling between q$P$ and q$SP$.

## CONCLUSIONS

Velocity gradients in anisotropic media lead to complications in the analysis of anisotropic wave propagation. The ray equations are particularly useful for studying these phenomena, and can be used to predict various amplitude and polarization anomalies and patterns of shear-wave splitting. Strong anisotropy can cause unusual effects, such as ray paths which have three turning points in laterally homogeneous models. Perhaps the most important result of this work is that quasi-shear wave polarizations typically twist along ray paths within gradients in anisotropic media. The twisting results in frequency-dependent coupling between the q$S$-waves, which is especially strong near singularities in the q$S$-wave polarizations. Paper II discusses this coupling in detail, and shows how it often must be taken into account to correct ray theory results.

## ACKNOWLEDGEMENTS

We thank Dr S. Crampin and two anonymous reviewers for their comments. This research was partially supported by Shell UK Exploration and Production. Department of Earth Sciences contribution number 1239.

## REFERENCES

Anderson, D. L., Minster, B. & Cole, D., 1974. The effect of oriented cracks on seismic velocities, *J. geophys. Res.*, **79**, 4011–4015.

Ando, M., 1984. ScS polarization anisotropy around the Pacific Ocean, *J. Phys. Earth*, **32**, 179–195.

Ando, M., Ishikawa, Y. & Yamazaki, F., 1983. Shear wave polarization anisotropy in the upper mantle beneath Honshu, Japan, *J. geophys. Res.*, **88**, 5850–5864.

Au, C. Y. D. & Clowes, 1982. Crustal structure from an ocean bottom seismometer survey in the Nootka fault zone off western Canada, *Geophys. J. R. astr. Soc.*, **68**, 27–47.

Backus, G. E., 1970. A geometric picture of anisotropic elastic tensors, *Rev. Geophys. Space Phys.*, **8**, 633–671.

Backus, G. E., 1982. Reply: limits of validity of first-order perturbation theory for quasi-P velocity in weakly anisotropic media, *J. geophys. Res.*, **87**, 4641–4644.

Bamford, D., 1977. Pn velocity anisotropy in a continental upper mantle, *Geophys. J. R. astr. Soc.*, **49**, 29–48.

Booth, D. C. & Crampin, S., 1983. The anisotropic reflectivity technique: theory, *Geophys. J. R. astr. Soc.*, **72**, 755–766.

Booth, D. C. & Crampin, S., 1985. Shear-wave polarizations on a curved wave-front at an isotropic free surface, *Geophys. J. R. astr. Soc.*, **83**, 31–45.

Booth, D. C., Crampin, S., Evans, R. & Roberts, G., 1985. Shear-wave polarizations near the North Anatolian Fault-I. Evidence for anisotropy-induced shear-wave splitting, *Geophys. J. R. astr. Soc.*, **83**, 61–73.

Červený, V., 1972. Seismic rays and ray intensities in inhomogeneous anisotropic media, *Geophys. J. R. astr. Soc.*, **29**, 1–13.

Červený, V. & Firbas, P., 1984. Numerical modelling and inversion of travel times of seismic body waves in inhomogeneous ansiotropic media, *Geophys. J. R. astr. Soc.*, **76**, 41–51.

Červený, V., Molotkov, I. A. & Pšenčík, I., 1977. *Ray Method in Seismology*, Univerzita Karlova, Praha.

Chapman, C. H. & Shearer, P. M., 1988. Ray tracing in azimuthally anisotropic media—II. Quasi-shear wave coupling, *Geophys. J.*, **96**, 65–83.

Crampin, S., 1981. A review of wave motion in anisotropic and cracked elastic-media, *Wave Motion*, **3**, 343–391.

Crampin, S., 1984. Effective elastic constants for wave propagation through cracked solids, *Geophys. J. R. astr. Soc.*, **76**, 135–145.

Crampin, S. & Booth, D. C., 1985. Shear-wave polarizations near the North Anatolian Fault—II. Interpretations in terms of crack-induced anisotropy, *Geophys. J. R. astr. Soc.*, **83**, 75–92.

Crampin, S. & King, D. W., 1977. Evidence for anisotropy in the upper mantle beneath Eurasia from generalized higher mode surface waves, *Geophys. J. R. astr. Soc.*, **49**, 59–85.

Crampin, S. & Yedlin, M., 1981. Shear-wave singularities of wave propagation in anisotropic media, *J. Geophys.*, **49**, 43–46.

Crampin, S., Evans, R., Ücer, B., Dolye, M., Davis, J. P., Yegorkina, G. V. & Miller, A., 1980. Observations of dilatancy-induced polarization anomalies and earthquake prediction, *Nature*, **286**, 874–877.

Crampin, S., Stephen, R. A. & McGonigle, R., 1982. The polarization of *P*-waves in anisotropic media, *Geophys. J. R. astr. Soc.*, **68**, 477–485.

Crampin, S., Booth, D. C., Krasnova, M. A., Chesnokov, E. M., Maximov, A. B. & Tarasov, N. T., 1986. Shear-wave polarizations in the Peter the First Range indicating crack-induced anisotropy in a thrust-fault regime, *Geophys. J. R. astr. Soc.*, **84**, 401–412.

Crampin, S., McGonigle, R. & Ando, M., 1986. Extensive-dilatancy anisotropy beneath Mount Hood, Oregon and the effect of aspect ratio on seismic velocities through aligned cracks, *J. geophys. Res.*, **91**, 12703–12710.

Duff, G. F. D., 1960. The Cauchy problem of elastic waves in an anisotropic medium, *Phil. Trans. R. Soc. A*, **252**, 249–273.

Forsyth, D. W., 1975. The early structural evolution and anisotropy of the oceanic upper mantle, *Geophys. J. R. astr. Soc.*, **43**, 103–162.

Fryer, G. J. & Frazer, L. N., 1984. Seismic waves in stratified anisotropic media, *Geophys. J. R. astr. Soc.*, **78**, 691–710.

Gajewski, D. & Pšenčík, I., 1987. Computation of high-frequency seismic wave-fields in 3-D laterally inhomogeneous anisotropic media, *Geophys. J. R. astr. Soc.*, **91**, 383–411.

Garmany, J., 1983. Some properties of elastodynamic eigensolutions in stratified media, *Geophys. J. R. astr. Soc.*, **75**, 565–569.

Garmany, J., 1988a. Seismograms in stratified anisotropic media—I. WKBJ theory, *Geophys. J.*, **92**, 365–377.

Garmany, J., 1988b. Seismograms in stratified anisotropic media—II. Uniformly asymptotic approximations, *Geophys. J.*, **92**, 379–389.

Hanyga, A., 1986. Gaussian beams in anisotropic elastic media, *Geophys. J. R. astr. Soc.*, **85**, 473–503.

Hess, H. H., 1964. Seismic anisotropy of the uppermost mantle under oceans, *Nature*, **203**, 629–631.

Hudson, J. A., 1980. Overall properties of a cracked solid, *Math. Proc. Camb. phil. Soc.*, **88**, 371–384.

Hudson, J. A., 1981. Wave speeds and attenuation of elastic waves in material containing cracks, *Geophys. J. R. astr. Soc.*, **64**, 133–150.

Keith, C. M. & Crampin, S., 1977. Seismic body waves in anisotropic media: reflection and refraction at a plane interface. *Geophys. J. R. astr. Soc.*, **49**, 181–208.

Kirkwood, S. C. & Crampin, S., 1981. Surface-wave propagation in an ocean basin with an anisotropic upper-mantle: observations of polarization anomalies, *Geophys. J. R. astr. Soc.*, **64**, 487–497.

Leary, P. C., Li, Y.-G., & Aki, K., 1987. Observation and modelling of fault-zone fracture seismic anisotropy—I. *P*, *SV* and *SH* travel times, *Geophys. J. R. astr. Soc.*, **91**, 461–484.

Li, Y.-G., Leary, P. C., & Aki, K., 1987. Observation and modelling of fault-zone fracture seismic anisotropy—II. *P*-wave polarization anomalies, *Geophys. J. R. astr. Soc.*, **91**, 485–492.

Mitchell, B. J. & Yu, G.-K., 1980. Surface wave dispersion, regionalized velocity models, and anisotropy of the Pacific crust and upper mantle, *Geophys. J. R. astr. Soc.*, **63**, 497–514.

Morelli, A., Dziewonski, A. M. & Woodhouse, J. H., 1986. Anisotropy of the inner core inferred from PKIKP travel times, *Geophys. Res. Lett.*, **13**, 1545–1548.

Musgrave, M. J. P., 1970. *Crystal Acoustics*, Holden-Day, San Francisco.

Payton, R. G., 1983. *Elastic Wave Propagation in Transversely Isotropic Media*, Martinus Nijhoff, The Hague.

Raitt, R. W., Shor, G. G., Francis, T. J. G. & Morris, G. B., 1969. Anisotropy of the Pacific upper mantle, *J. geophys. Res.*, **74**, 3095–3109.

Shearer, P. M. & Chapman, C. H., 1988. Ray tracing in anisotropic media with a linear gradient, *Geophys. J.*, **94**, 575–580.

Shearer, P. M. & Orcutt, J. A., 1985. Anisotropy in the oceanic lithosphere—theory and observations from the Ngendei seismic refraction experiment in the southwest Pacific, *Geophys. J. R. astr. Soc.*, **80**, 493–526.

Shearer, P. M. & Orcutt, J. A., 1986. Compressional and shear wave anisotropy in the oceanic lithosphere—the Ngendei seismic refraction experiment, *Geophys. J. R. astr. Soc.*, **87**, 967–1003.

Shimamura, H., 1984. Anisotropy in the oceanic lithosphere of the Northwestern Pacific Basin, *Geophys. J. R. astr. Soc.*, **76**, 253–260.

Singh, S. & Chapman, C. H., 1986. Shear waveforms at and near cusps in anisotropic media, *Eos, Trans. Am. geophys. Un.*, **67**, 1116.

Stephen, R. A., 1981. Seismic anisotropy observed in the oceanic crust, *Geophys. Res. Lett.*, **90**, 865–868.

Stephen, R. A., 1985. Seismic anisotropy in the upper oceanic crust, *J. geophys. Res.*, **90,** 11383–11396.
Tanimoto, T. & Anderson, D. L., 1985. Lateral heterogeneity and azimuthal anisotropy of the upper mantle: Love and Rayleigh waves 100–250 s, *J. geophys. Res.*, **90,** 1842–1858.
White, R. S. & Whitmarsh, R. B., 1984. An investigation of seismic anisotropy due to cracks in the upper oceanic crust at 45 °N, Mid-Atlantic Ridge, *Geophys. J. R. astr. Soc.*, **79,** 439–467.
Woodhouse, J. H., Giardini, D. & Li, X.-D. 1986. Evidence for inner core anisotropy from free oscillations, *Geophys. Res. Lett.*, **13,** 1549–1552.

## APPENDIX: EIGENSOLUTIONS FOR HEXAGONALLY SYMMETRIC MEDIA

The eigenvalues (phase velocities squared) and eigenvectors (polarizations) for anisotropic material with hexagonal symmetry may be obtained from relatively simple expressions. A short derivation of these expressions follows, using notation from Musgrave (1970) and Červený (1972).

Without loss of generality, we can choose reference axes such that the symmetry axis is the $x_3$ axis. For hexagonal symmetry, we have the following density normalized elastic constants:

$$a_{1111} = a_{2222}$$
$$a_{3333}$$
$$a_{1122}$$
$$a_{1133} = a_{2233}$$
$$a_{1313} = a_{2323}$$
$$a_{1212} = \tfrac{1}{2}(a_{1111} - a_{1122}). \tag{A1}$$

We wish to solve the characteristic equation

$$(a_{ijkl}\hat{p}_j\hat{p}_l - v^2\delta_{ik})\hat{g}_k = 0, \tag{A2}$$

where $\hat{\mathbf{p}}$ is the unit slowness direction, $\hat{\mathbf{g}}$ is the polarization unit vector and $v$ is the phase velocity. Following Musgrave (1970), let

$$a = a_{1111} - a_{2323}$$
$$c = a_{1111} - a_{1122} - 2a_{2323}$$
$$d = a_{1133} + a_{2323}$$
$$g = \tfrac{1}{2}(a_{1111} + a_{1122})$$
$$h = a_{3333} - a_{2323}$$
$$H = v^2 - a_{2323}. \tag{A3}$$

Substituting (A1) into (A2) and using (A3), we obtain

$$\begin{pmatrix} \hat{p}_1^2 a + \tfrac{1}{2}\hat{p}_2^2 c - H & \hat{p}_1\hat{p}_2 g & \hat{p}_1\hat{p}_3 d \\ \hat{p}_1\hat{p}_2 g & \tfrac{1}{2}\hat{p}_1^2 c + \hat{p}_2^2 a - H & \hat{p}_2\hat{p}_3 d \\ \hat{p}_1\hat{p}_3 d & \hat{p}_2\hat{p}_3 d & \hat{p}_3^2 h - H \end{pmatrix} \times \begin{pmatrix} \hat{g}_1 \\ \hat{g}_2 \\ \hat{g}_3 \end{pmatrix} = \begin{pmatrix} 0 \\ 0 \\ 0 \end{pmatrix}. \tag{A4}$$

Now let $m^2 = \hat{p}_1^2 + \hat{p}_2^2$ and $n^2 = \hat{p}_3^2$. Factorizing (A4), we obtain expressions for the three eigenvalues

$$H_{qSR} = \tfrac{1}{2}m^2 c \tag{A5}$$

$$H_{qP} = \tfrac{1}{2}\{m^2 a + n^2 h + [(m^2 a + n^2 h)^2 - 4n^2 m^2(ah - d^2)]^{1/2}\} \tag{A6}$$

$$H_{qSP} = \tfrac{1}{2}\{m^2 a + n^2 h - [(m^2 a + n^2 h)^2 - 4n^2 m^2(ah - d^2)]^{1/2}\}, \tag{A7}$$

where, following the notation of Crampin (1981), q$P$ indicates the quasi-compressional wave, q$SP$ indicates the quasi-shear wave with polarization within the symmetry plane, and q$SR$ indicates the quasi-shear wave with polarization orthogonal to the symmetry plane. In the case of a vertical symmetry axis (commonly referred to as transversely isotropic), q$SP$ and q$SR$ are equivalent to q$SV$ and q$SH$, respectively.

Corresponding phase velocities may be obtained from (A3). Polarizations are obtained by substituting the appropriate expression for $H$ into (A4).

### q*SR* polarization

$$\hat{g}_1 = -\frac{\hat{p}_2}{m}, \quad \hat{g}_2 = \frac{\hat{p}_1}{m}, \quad \hat{g}_3 = 0. \tag{A8}$$

### q*P* and q*SP* polarization

Define

$$k_m = H - n^2 h$$
$$k_n = mnd.$$

Then for $\hat{p}_3 > 0$,

$$\hat{g}_1 = \frac{k_m}{(k_m^2 + k_n^2)^{1/2}}\frac{\hat{p}_1}{m}, \quad \hat{g}_2 = \frac{k_m}{(k_m^2 + k_n^2)^{1/2}}\frac{\hat{p}_2}{m}, \quad \hat{g}_3 = \frac{k_n}{(k_m^2 + k_n^2)^{1/2}}. \tag{A9}$$

At $m = 0$, the q$P$ polarization is (0,0,1), while the q$SP$ and q$SR$ polarizations are undefined within the plane perpendicular to (0,0,1). At $n = 0$, then $m = 1$ and the q$P$ polarization is $(\hat{p}_1, \hat{p}_2, 0)$, the q$SR$ polarization is $(-\hat{p}_2, \hat{p}_1, 0)$, and the q$SP$ polarization is (0,0,1). When $\hat{p}_3 < 0$, care must be taken to ensure polarization continuity at $\hat{p}_3 = 0$. This can be done for q$P$-waves by switching the sign of $\hat{g}_3$, and for q$SP$-waves by switching the signs of $\hat{g}_1$ and $\hat{g}_2$ in the above expressions.

Equations (A8) and (A9) are equivalent to similar expressions in Musgrave (1970) and Hanyga (1986), but are more numerically stable near $n = 0$. Also note the typographical error in Hanyga (1986) equation (G15); the $C'$ should be $A'$. With a suitable rotation of coordinates, these expressions can be used to find the phase velocity and polarization for a hexagonally symmetric material with any symmetry axis orientation.